Chemical Engineering Science 301 (2025) 120693

Contents lists available at ScienceDirect

Chemical Engineering Science

journal homepage: www.elsevier.com/locate/ces

Probing the interaction mechanisms of lipid nanoparticle-encapsulated mRNA with surfaces of diverse functional groups: Implication for mRNA transport

Jingyi Wang [a,c,1], Jiawen Zhang [b,c,1], Sijia Li [c], Hui Qian [d], Dengfeng Liu [e], Isaias Prado [e], Sharon Wang [e], Akhilesh Bhambhani [e], Hongbo Zeng [c,*]

[a] *College of Chemistry and Chemical Engineering, Southwest Petroleum University, Chengdu, Sichuan 610500, China*
[b] *School of Materials Science and Engineering, Southeast University, Nanjing 211189, China*
[c] *Department of Chemical and Materials Engineering, University of Alberta, Edmonton, AB T6G 1H9, Canada*
[d] *Nanotechnology Research Center, National Research Council Canada, Edmonton, AB T6G 2M9, Canada*
[e] *Ultragenyx Pharmaceutical Inc., 5000 Marina Blvd, Brisbane, CA 94005, USA*

ARTICLE INFO

Keywords:
Intermolecular interactions
mRNA transport
Lipid nanoparticles
Functional groups

ABSTRACT

The transport of mRNA plays an indispensable role in vaccine drug delivery and emerging therapies. The attachment of lipid nanoparticle encapsulating mRNA (mRNA-LNP) to biological and engineering surfaces is determined by their intermolecular and surface interactions. In this work, the interactions between mRNA-LNP and surfaces with various functional groups were investigated using atomic force microscopy. The results show that mRNA chains are coiled in LNPs, and the surface charges of mRNA are screened by the surrounding lipid molecules. Approach force curves demonstrate that the steric repulsion varies with functional groups. Force mapping reveals that the intermolecular interactions, i.e., hydrogen bonding and electrostatic interaction, contribute to the adhesion. The –OH group is suggested as the most probable binding site for mRNA-LNP attachment. This work provides new insights into mRNA transport mechanisms at biological and engineering surfaces, with useful implications for designing novel nanocarriers and developing functional surfaces for biological applications.

1. Introduction

The transport of mRNA into cells as a therapeutic drug has been under development since 1989 (Malone et al., 1989). Once the mRNA molecules are delivered to the cytosol of target cells, the translation of messages on mRNA molecules begins at the ribosomes for protein synthesis. Such translation of genetic information and production of encoded proteins could train the immune system to react to the attack of like proteins. This functional principle of mRNA vaccines has been widely applied to defend against the recent COVID-19 (Hou et al., 2021; Schoenmaker et al., 2021; Zhang et al., 2020; Kisby et al., 2021). The mRNA molecules are encapsulated in carriers or vectors, such as liposomes or lipid nanoparticles (LNP), for improving delivery efficiency, where the mRNA stability, targeting ability, and penetrating ability through the cell membrane are enhanced (Yin et al., 2014; Buschmann et al., 2021; Yan et al., 2017; Peng and Wagner, 2019). In order to transport mRNA, the LNP-encapsulated mRNA (mRNA-LNP) needs to interact with the target cell surface for endocytosis; the uptake efficiency is governed by the intermolecular and surface interactions. It has been reported that the cationic lipid vectors interact with the cell membrane through electrostatic interactions (del Pozo-Rodríguez et al., 2008; Zhang et al., 2017; Nakamura et al., 2020). The charges on the lipid vector and cell membrane were characterized by zeta potential measurement as positive and negative, respectively. Such interactions could also occur through specific ligand-receptor binding (Nakamura et al., 2020; Gan et al., 2013; Apaolaza et al., 2016), a much stronger interaction than the hydrophobic interaction, as indicated by surface force apparatus (SFA) measurement (Helm et al., 1991; Wong et al., 1997; Jeppesen et al., 2001). Such strong interaction is the summation of the interactions of multiple binding sites between the ligand and receptor,

---

[*] Corresponding author.
E-mail address: hongbo.zeng@ualberta.ca (H. Zeng).
[1] J. Wang and J. Zhang contributed equally to this work.

https://doi.org/10.1016/j.ces.2024.120693
Received 20 July 2024; Received in revised form 23 August 2024; Accepted 31 August 2024

and probably includes chemical bonding, hydrogen bonding, van der Waals force, hydrophobic force, etc. (Zhang et al., 2003; van Oss, 2000). The transport process of mRNA-LNP may also include the adsorption on the surfaces of medical devices (Li, 2017), filtration membranes (Messerian et al., 2023), inorganic materials (Mager, 2009), and biological molecules (Zhang et al., 2021). Those surfaces have different physiochemical properties and contain diverse functional groups, which influence the interactions between mRNA-LNP and surfaces and ultimately control the adsorption process. However, the role of functional groups on the biological and non-biological surfaces in determining their interactions with mRNA-LNP is still unclear. Consequently, elucidating the ambiguous underlying interaction mechanisms of mRNA-LNP with the surfaces of diverse functional groups is crucial for understanding the transport process and the design of efficient nanocarriers for mRNA delivery.

Atomic force microscopy (AFM) is a powerful tool for quantitatively measuring the interaction forces and nanomechanical properties (Garcia-Manyes and Sanz, 2010, 1798,; Wang et al., 2016; Park et al., 2020; Kulkarni et al., 2022; Wang et al., 2024; Hu et al., 2022). Because of the small area on the AFM tip apex and the capability of manipulating molecules on the AFM tip for functionalization, AFM is ideal for measuring interaction forces between biomolecules (Kumar and Li, 2010; Turasan and Kokini, 2017; Inkinen et al., 2011). The retracting force curves that are measured after the contact of two surfaces/molecules could provide the adhesion or unbinding force, which is useful for analyzing the specific interactions between biomolecules. There has been limited research to demonstrate the application of AFM in measuring the interaction forces involving RNA or LNP (Wang et al., 2023; Szebeni et al., 2023; de Chateauneuf-Randon et al., 2024). A few key findings from siRNA and lipid compositional studies using AFM are described here, illustrating the significance of AFM in understanding molecular-level interactions (Szebeni et al., 2023; Dumitru et al., 2015; Dumitru et al., 2018). Dumitru et al. (Dumitru et al., 2015), for example, studied the interactions between siRNA and polyamidoamine (PAMAM) dendrimers using AFM to understand the efficiency of the PAMAM carriers for siRNA delivery. The retracting force curves between siRNA modified AFM tip and PAMAM dendrimers showed three types of unbinding events with the unbinding forces of 28 pN, 38 pN and 50 pN, respectively, corresponding to different electrostatic interactions between positively charged dendrimers and negatively charged phosphate groups on siRNA. The study finding suggested that the siRNA interacted with two amino branches of one dendrimer or with one amino branch of each of the two adjacent dendrimers. Similarly, Dumitru et al. demonstrated that the functionalized AFM tips could be applied to differentiate the lipid compositions by measuring the adhesion force (Dumitru et al., 2018). Due to the specific interactions between the functionalized AFM tip and sphingomyelin- or cholesterol-enriched lipid domains within 1,2-dioleoyl-*sn*-glycero-3-phosphocholine, the adhesion forces on the sphingomyelin domains and cholesterol domains were different, and the two domains were distinguishable on the adhesion maps. In addition to the retracting forces curves that could obtain adhesion forces, the approaching force curves could quantify the surface forces during attachment. Szebeni et al. (Szebeni et al., 2023) applied sharp silicone AFM tips to measure the mechanical properties of mRNA-loaded Comirnaty LNPs. The results revealed that the AFM tip can penetrate the LNP structure and the encapsulated mRNA can be pulled out from the LNP as characterized by the sawtooth-like force profile during tip retraction. To our knowledge, there is no publication on the study of interactions between mRNA-LNP and the surface with varying functional groups. In this work, AFM tips were modified with different functional groups. The force-separation curves and the adhesion histograms were analyzed and compared to investigate the different roles of these functional groups. The interaction mechanisms of mRNA-LNP with the surfaces of functional groups are proposed and the most possible binding sites for mRNA-LNP attachment are suggested. This work will have implications for the interaction of mRNA-LNP with various surfaces, such as cell membrane, medical device and filtration membrane, which exist during the storage, transport and therapeutic processes. The role of possible functional groups on those surfaces for mRNA-LNP attachment will be comprehensively discussed.

2. Experimental section

2.1. Materials

mRNA and mRNA-LNP samples were provided by Ultragenyx Pharmaceutical (Brisbane,CA, US). PBS buffer, 11-mercaptoundecanoic acid ($HS(CH_2)_{10}COOH$, 98 %), 11-mercapto-1-undecanol ($HS(CH_2)_{10}CH_2OH$, 99 %), 11-amino-1-undecanethiol hydrochloride ($HS(CH_2)_{10}CH_2NH_2$, 99 %), 11-mercaptoundecylphosphonic acid ($HS(CH_2)_{10}CH_2PO_3H_2$, 95 %), and 1-undecanethiol ($HS(CH_2)_{10}CH_3$, 98 %) were purchased from Sigma-Aldrich. Mica sheets were purchased from S & J Trading Inc. (Glen Oaks, NY, USA). Milli-Q water was used in preparing aqueous solutions and rinsing process (Millipore deionized, 18.2 MΩ·cm resistivity).

2.2. Characterization of mRNA and mRNA-LNP

The morphology of mRNA-LNP was characterized using cryogenic transmission electron microscopy (cryo-TEM). Cryo-TEM specimens of mRNA-LNP were prepared using rapid freezing method (Qian, 2021; Qian et al., 2021). Briefly, one 4 μL droplet of 1 μg/mL mRNA-LNP solution (diluted from 1 mg/mL mRNA-LNP solution with Milli-Q water) was placed on a lacey carbon TEM grid pretreated with glow discharge. Excess solution was blotted using filter paper from the back side of the TEM grid, and then the TEM grid was rapidly plunged into liquid ethane at −180 °C. The frozen mRNA-LNP specimen was kept in liquid nitrogen and transferred for cryo-TEM imaging. In this way, the image of mRNA-LNPs embedded in vitreous ice was achieved.

The morphologies and surface structures of mRNA-LNP and mRNA were also characterized by AFM imaging. The mRNA-LNP solution (~20 μL) was dropped on a freshly cleaved mica surface for 10 min incubation. Then the mica surface was blow-dried with nitrogen gas. The obtained mRNA-LNP-coated mica was further dipped in Milli-Q water to wash away the loosely attached mRNA-LNPs. The sample of mRNA on mica was prepared by pre-treating the mica surface with 20 mM $MgSO_4$ solution for 3 min, dropping the mRNA solution (1 μg/mL, ~10 μL) onto the mica surface for 10 min incubation, washing with Milli-Q water, and then blowing dry the surface with nitrogen gas. Because mRNA carries more negative charges than mRNA-LNP, the introduction of Mg^{2+} could help fix mRNA on negatively charged mica, possibly through electrostatic interaction or complexation (Neaves et al., 2009; Kretov et al., 2015). The high-resolution AFM images were acquired in air under tapping mode on a Dimension Icon AFM (Bruker, Santa Barbara, CA, USA). The AFM tips used for imaging were RTESP-150 (Bruker).

The size distribution (using dynamic light scattering (DLS) technique) and zeta potential measurements of mRNA-LNP and mRNA were conducted on a Zetasizer Nano ZSP (Malvern Instrument Ltd.). The concentration of mRNA-LNP and mRNA solutions was 10 μg/mL. The measurement under the same condition was repeated three times and an average value was reported.

2.3. Force measurements using AFM

The force measurements were conducted between mRNA-LNP and various functional groups in PBS solution on an MFP-3D AFM (Asylum Research, Santa Barbara, CA, USA). The PBS solution has a pH of 7.4 and is commonly used in biological research as it is isotonic and non-toxic to most cells. The mRNA-LNP surface was prepared using the same procedure as that for preparing the AFM imaging sample. The AFM gold coated tips (NPG-10, Bruker) were treated with UV/Ozone for 30 min.

The cleaned tips were then immersed in 10 mM 11-mercaptoundecanoic acid, 11-mercapto-1-undecanol, 11-amino-1-undecanethiol hydrochloride, 11-mercaptoundecylphosphonic acid, and 1-undecanethiol in ethanol solutions overnight for obtaining –COOH, –OH, $-NH_2$, $-PO_3H_2$, and $-CH_3$ groups functionalized AFM tips, respectively. This tip functionalization process was well established in the literature and in our previous studies (Frisbie et al., 1994; Xie et al., 2017; Xie et al., 2020). In this study, the successful tip functionalization was confirmed by measuring the water contact angle and X-ray photoelectron spectroscopy (XPS) of functionalized gold surface, and the results were shown in Figs. S1–S6. Before use, the functionalized AFM tips were rinsed with ethanol and Milli-Q water and dried with nitrogen gas. The functionalized tip was advanced toward and then retracted from the mRNA-LNP surface to record the approaching and retracting force-separation curves, respectively. A schematic of the AFM setup for force measurement between a functionalized AFM tip and an mRNA-LNP is shown in Fig. 1.

The conical AFM tip with a pyramidal geometry and a spherical cap at the apex (Fig. 1) was considered for solving the interacting forces of conical tip-flat surface system. Then the van der Waals force F_{vdw} is given by (Xie et al., 2020; Drelich et al., 2007; Wang et al., 2017):

$$F_{vdw} = \frac{A}{6}\left[\frac{R+D-2L}{L^2} - \frac{R-D}{D^2}\right] - \frac{A}{3\tan^2\alpha}\left[\frac{1}{L} + \frac{R\sin\alpha\tan\alpha - D - R(1-\cos\alpha)}{2L^2}\right] \tag{1}$$

where A is the Hamaker constant, R is the radius of the spherical cap at the tip apex, D is the separation distance between tip and flat surface, and α and β are the geometrical angles shown in Fig. 1 with $\alpha + \beta = 90^\circ$, and $L = D + R(1 - \cos\alpha)$. The steric force F_{steric} can be described by an exponential expression (Butt et al., 1999):

$$F/R = C\exp(-D/D_0) \tag{2}$$

here C is the pre-exponential parameter, and D_0 is the decay length. Thus, the total surface force is:

$$F_{\text{total}} = F_{\text{vdw}} + F_{\text{steric}} \tag{3}$$

The interaction forces on mica surface include hydration force, which also has an exponential expression (Israelachvili and Wennerstroem, 1992) as shown in Equation (2). However, the steric force decays faster than the hydration force, as the steric barrier for steric force (lipid molecules) has larger dimension than that for hydration force (water molecules).

3. Results and discussion

3.1. Surface morphology and nanostructure

Fig. 2a–d represent the morphologies and structures of mRNA-LNP and mRNA characterized using cryo-TEM and AFM. Fig. 2a is the cryo-TEM image showing the morphology of mRNA-LNP embedded in vitreous ice. The low temperature kept the mRNA-LNPs from being damaged by the electron beam. The diameters of the spherical mRNA-LNPs are tens of nanometers with a Gaussian fitting peak at 30.14 nm with a wide span of 10–60 nm (Fig. 2d). The morphology of mRNA-LNP was also characterized using AFM imaging. In the tapping mode AFM imaging, an AFM tip scanned over the surface and recorded the surface contour without damaging the mRNA-LNPs. The AFM image in Fig. 2b presents a particle morphology similar to that shown in Fig. 2a. The corresponding size (diameter) distribution has a peak at 33.33 nm (Fig. 2e), which is similar to that derived from cryo-TEM image.

The mRNA molecules have a distinguishable morphology from mRNA-LNP. As demonstrated in Fig. 2c, the mRNA chains are extended, and some of them stack together forming RNA secondary/tertiary structures. The size distribution of mRNA (Fig. 2f) is plotted by calculating the surface area and diameter of a particle by considering a circular area that the particle occupied. Thus, the high aspect ratio of mRNA and the formation of secondary/tertiary structures result in a larger statistical size of mRNA than that of mRNA-LNP.

The high-resolution AFM topographic and phase images of mRNA-LNP (Fig. 3) provide the details of a single mRNA-LNP. The cross-section line profiles 1 and 2 illustrate the dimensions of the ellipsoid as ~35 nm and ~40 nm, respectively, while the height of the mRNA-LNP is only several nanometers, indicating a flat ellipsoid morphology of the mRNA-LNP on the mica surface. The spikes on the line profiles imply the presence of nanostructures in the mRNA-LNP. The phase image clearly demonstrates that the ring-shaped molecules are encapsulated in the lipid particle. The oscillation of AFM tip in tapping mode can be modulated by the mechanical properties of sample surface, which results in the phase shift of oscillation. Regions with different mechanical properties can be distinguished using the contrast of the phase image. The phase angle of the encapsulated molecules is comparable to the surrounding mica surface, which suggests similar rigidities of the

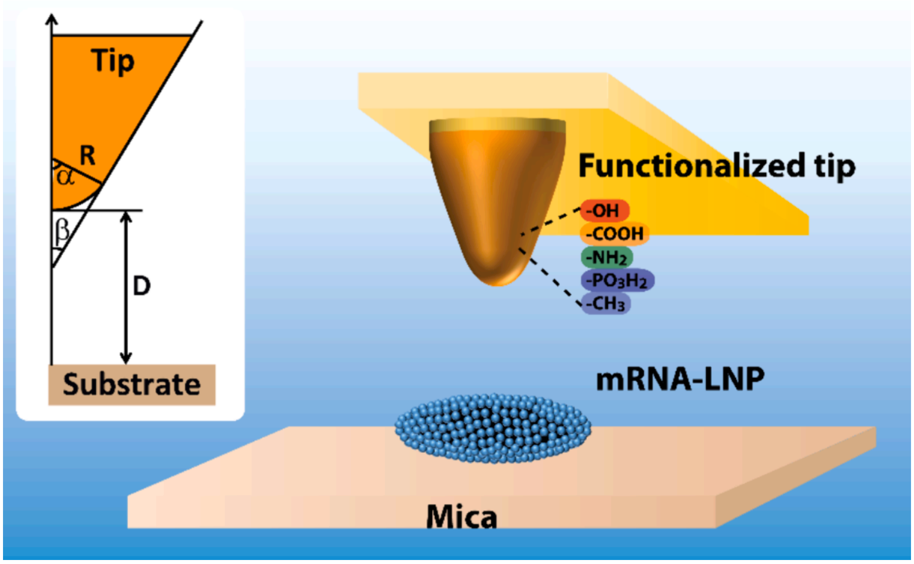

Fig. 1. Schematic illustrations of AFM force measurement setup and conical AFM tip geometry.

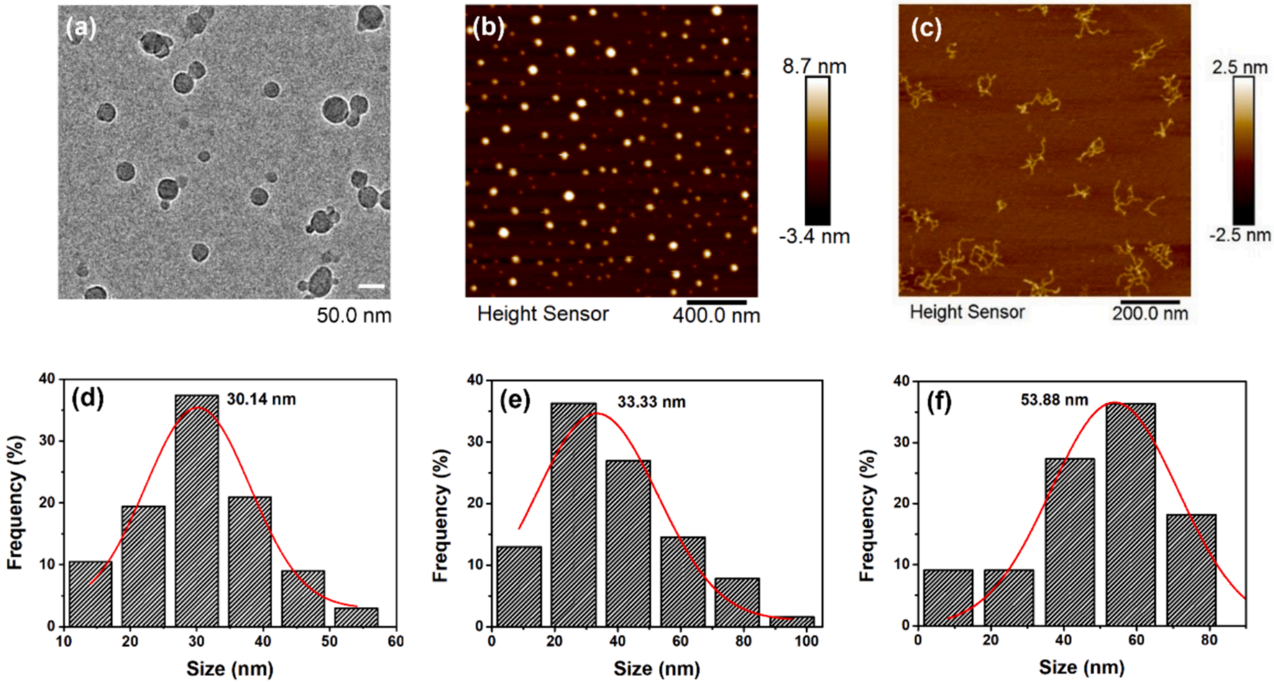

Fig. 2. (a) Cryo-TEM image of mRNA-LNP embedded in vitreous ice. (b) Topographic AFM image of mRNA-LNP. (c) Topographic AFM image of mRNA. (d), (e) and (f) The corresponding particle size distributions for (a), (b) and (c), respectively. The red lines are the Gaussian fitting curves of the size distributions.

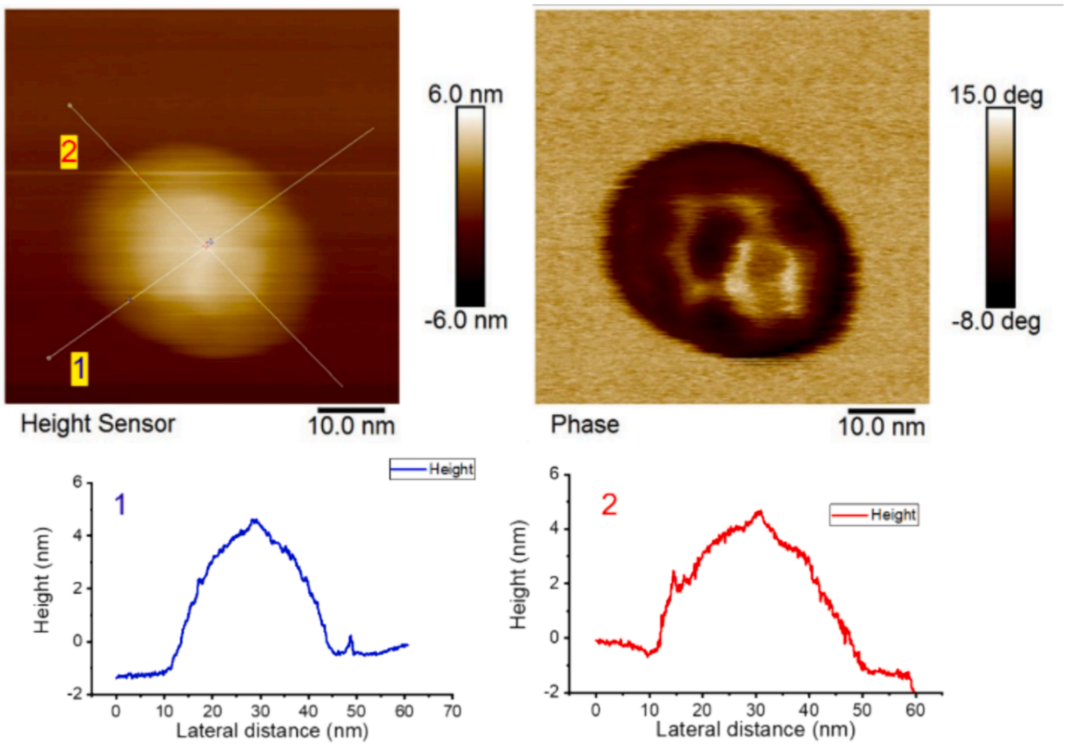

Fig. 3. AFM topographic and phase images of mRNA-LNP, which clearly show the configuration of the encapsulated mRNA.

molecules and mica. A comparison of the phase image of mRNA (Fig. 4b and e) with the molecules of rigidity similar to mica in the phase image of Fig. 3 leads to the conclusion that the molecules must be the mRNA molecules encapsulated in the LNP. The phase angle of the LNP is much smaller than that of mRNA or mica, characterizing the lower rigidity of the LNP compared to the rigidity of mRNA or mica. The high-resolution AFM topographic images of mRNA (Fig. 4a and d) illustrate that the mRNA chains have extended configurations with a length greater than 100 nm, and the height of the mRNA chains is ~912 pm. Once encapsulated in the LNPs, the mRNA molecules are coiled and surrounded by the lipid molecules to construct the spherical/ellipsoidal mRNA-LNPs.

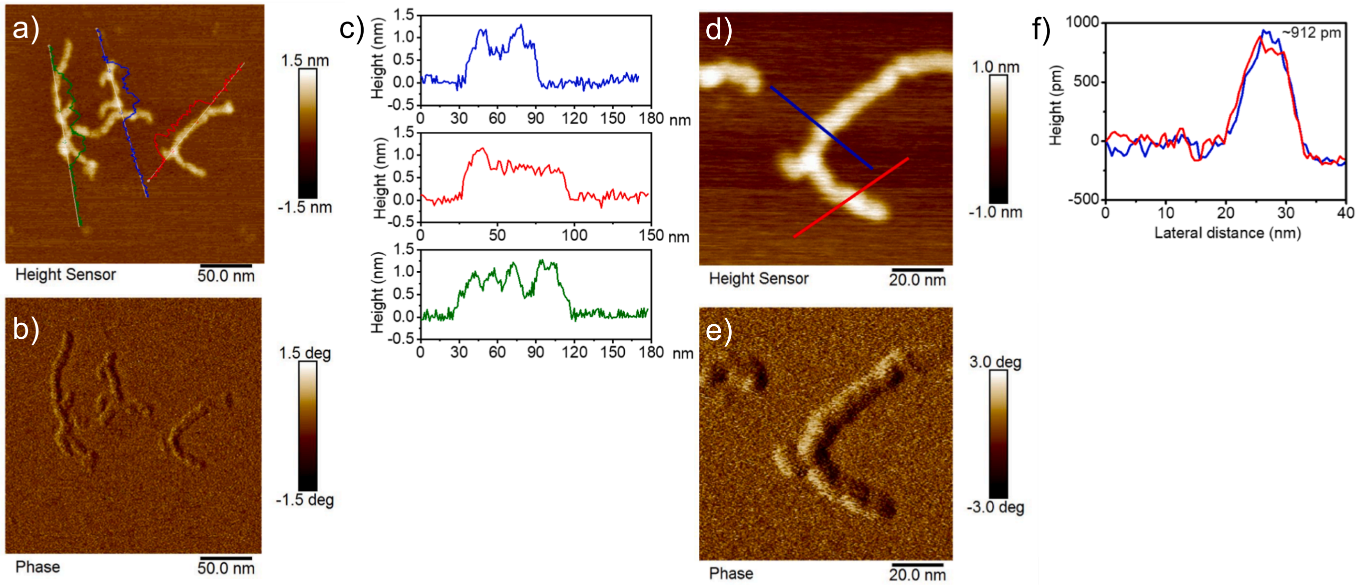

Fig. 4. (a) (d) AFM topographic and (b) (e) phase images of mRNA on mica substrates. (c) and (f) show the height profiles of mRNA chains.

3.2. Particle size and zeta potential in solution

The sizes of mRNA-LNP and mRNA in solution were measured by DLS technique using Zetasizer Nano ZSP. The average size of mRNA-LNP, based on three measurements, is ∼137.1 nm, as shown in Fig. 5a, which is larger than the size determined by Cryo-TEM and AFM (Fig. 2d and e). This is probably because of the aggregation of particles in solution or difference in the experimental techniques, as DLS technique characterizes hydrodynamic radius, which is usually larger than that observed using imaging techniques. The average zeta potential of mRNA-LNP is ∼−8.3 mV (Fig. 5b), suggesting a low charge density on the lipid particle surface and the subsequently weak electrical double layer repulsion between particles. Thus, the particles can aggregate through van der Waals attraction. The size of mRNA is 40–300 nm, and the average size, based on three measurements, is ∼106.0 nm (Fig. 5a). The length of mRNA measured in the AFM images (Fig. 4) falls in this range. The zeta potential of mRNA is ∼−57.0 mV (Fig. 5b), which leads to a strong electrical double layer repulsion between mRNA molecules and consequently the reduced probability of mRNA entanglement and aggregation. After the mRNAs are encapsulated in lipid particles, the surface charge of mRNA is screened by the lipid layers, resulting in a lowered absolute value of zeta potential.

3.3. Surface forces between mRNA-LNP and functionalized AFM tip

The interaction forces between mRNA-LNP and functionalized AFM tips in PBS pH 7.4 were measured. The self-assembly of thiols on the gold tip provides various functional groups, i.e., –COOH, –OH, $-NH_2$, $-PO_3H_2$, and $-CH_3$, which are typical functional groups on the surfaces and are found in biomolecules, e.g., –COOH, –OH, $-NH_2$ and $-CH_3$ in protein, –OH and $-CH_3$ in cholesterol, –OH in carbohydrate, and $-PO_4^-$- and $-CH_3$ in phospholipid. The $-PO_3H_2$ group is akin to $-PO_4^-$-, as $-PO_3H_2$ can represent the surface ionization status of $-PO_4^-$- at various pH (Zhang et al., 2000). After thiol modification, the gold surface exhibited increased water contact angle (Fig. S1). The $-CH_3$ surface had a contact angle ∼92° showing the hydrophobic nature of the surface. The other thiol modified surfaces maintained the hydrophilic property due to the exposure of polar groups. All the XPS spectra of thiol functionalized surfaces presented the S2p peak indicating the adsorption of thiol molecules on the surface (Figs. S2–S6). The pronounced O1s peaks were found in the –COOH, –OH and $-PO_3H_2$ samples. The $-NH_2$ and $-PO_3H_2$ surfaces showed N1s and P1s peaks, respectively. Force maps in a 2 × 2 μm^2 area with 400 force measurements were obtained, and the force curves were recorded. Three force maps were acquired for each experimental condition. The good distribution of mRNA-LNP on the

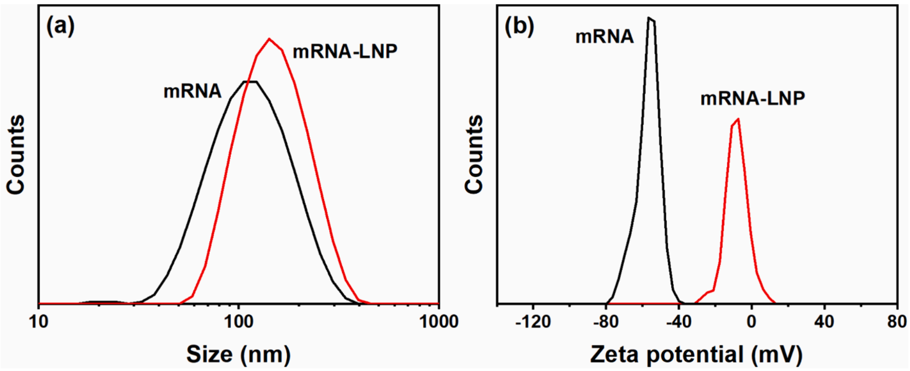

Fig. 5. (a) Size distributions of mRNA-LNP and mRNA measured by DLS technique. The average size, based on three measurements, is ∼137.1 nm for mRNA-LNP and ∼106.0 nm for mRNA. (b) Zeta potential distributions of mRNA-LNP and mRNA. The average zeta potential of the three measurements is ∼−8.3 mV for mRNA-LNP and ∼−57.0 mV for mRNA.

surface and the relatively big tip radius of ~30 nm facilitated the measurements of force curves on the mRNA-LNPs. To further exclude the influence of the mica surface, the interaction forces were also recorded on freshly cleaved mica surface, and the true interaction forces on mRNA-LNP can be recognized by comparing the forces measured on the mRNA-LNP sample and on the mica surface. The major differences in the interactions of functionalized tip with the mRNA-LNP sample and with mica are the surface and adhesion forces, which will be discussed in the following sections.

The approaching force-separation curves are shown in Fig. 6. In PBS pH 7.4, the ion concentration is 0.15 M, the Debye length of electrical double layer near the charged surface decreases, resulting in a screening effect of the electrical double layer force. The strength of van der Waals force is dependent on the Hamaker constant A_{132}, which is calculated as 2.7×10^{-20} J by using the combination correlation (Israelachvili, 2011):

$$A_{132} \approx (\sqrt{A_{11}} - \sqrt{A_{33}})(\sqrt{A_{22}} - \sqrt{A_{33}}) = \sqrt{A_{131}}(\sqrt{A_{22}} - \sqrt{A_{33}}) \qquad (4)$$

here the subscripts 1, 2 and 3 represent mRNA-LNP, gold and water, respectively. $A_{131} = 3 \times 10^{-21}$ J for the interactions of lipids (Israelachvili, 1994); $A_{22} = 45.5 \times 10^{-20}$ J and $A_{33} = 3.7 \times 10^{-20}$ J (Wang et al., 2016). In this calculation, the van der Waals force is predominantly determined by the Hamaker constant of the gold-water-LNP instead of the thiol-water-LNP at the separations larger than the thiol layer thickness (Israelachvili, 2011) on the gold tip ~1.7 nm (length of eleven C—C bonds). The van der Waals attraction does not dominate the interactions at small separations. A repulsive force arising at a separation of less than ~10 nm is observed as the dominant force. A similar repulsive force has been recognized as the steric force when measuring interaction forces on lipid bilayers and mRNA-LNPs (Szebeni et al., 2023; de Chateauneuf-Randon et al., 2024; Pera et al., 2004). In this case, the steric force originates from the compression of the protruded polyethylene glycol (PEG) lipid and possibly the further compression of other lipid components on the surface of mRNA-LNP. The steric repulsive force on mRNA-LNP is obviously different from the hydration repulsive force measured on the pure mica surface as shown in Fig. 7 in terms of both force range and force intensity, although the same exponential correlation is used for the theoretical calculation. The hydration force on mica originates from the ordering of water molecules adjacent to the super hydrophilic mica surface. The decay length of hydration force between functionalized AFM tips and mica varies with the affinity of the functional groups to water molecules as –COOH>–OH ≈ –NH_2 >

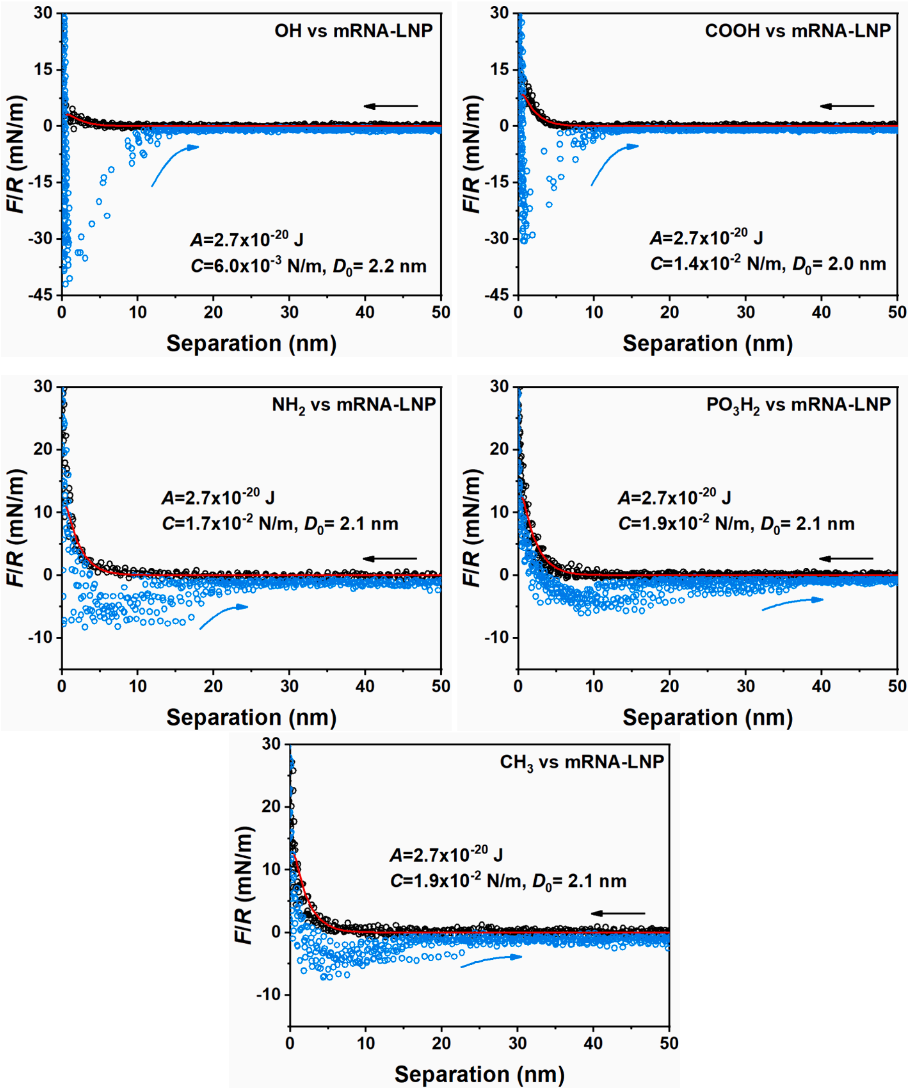

Fig. 6. Typical force-separation curves of interactions between mRNA-LNP surface and functionalized AFM tips in PBS pH 7.4. The circles are the experimental data, and the lines are the theoretical calculation curves. In the theoretical calculation, van der Waals force and steric force contribute to the total force. The Hamaker constant $A = 2.7 \times 10^{-20}$ J. For the steric force, the pre-exponential parameter C is 6.0×10^{-3}N/m for –OH, 1.4×10^{-2}N/m for –COOH, 1.7×10^{-2}N/m for –NH_2, 1.9×10^{-2}N/m for –PO_3H_2, and 1.9×10^{-2}N/m for –CH_3, and the decay length D_0 is 2.1 ± 0.1 nm. Each panel shows ten force curves.

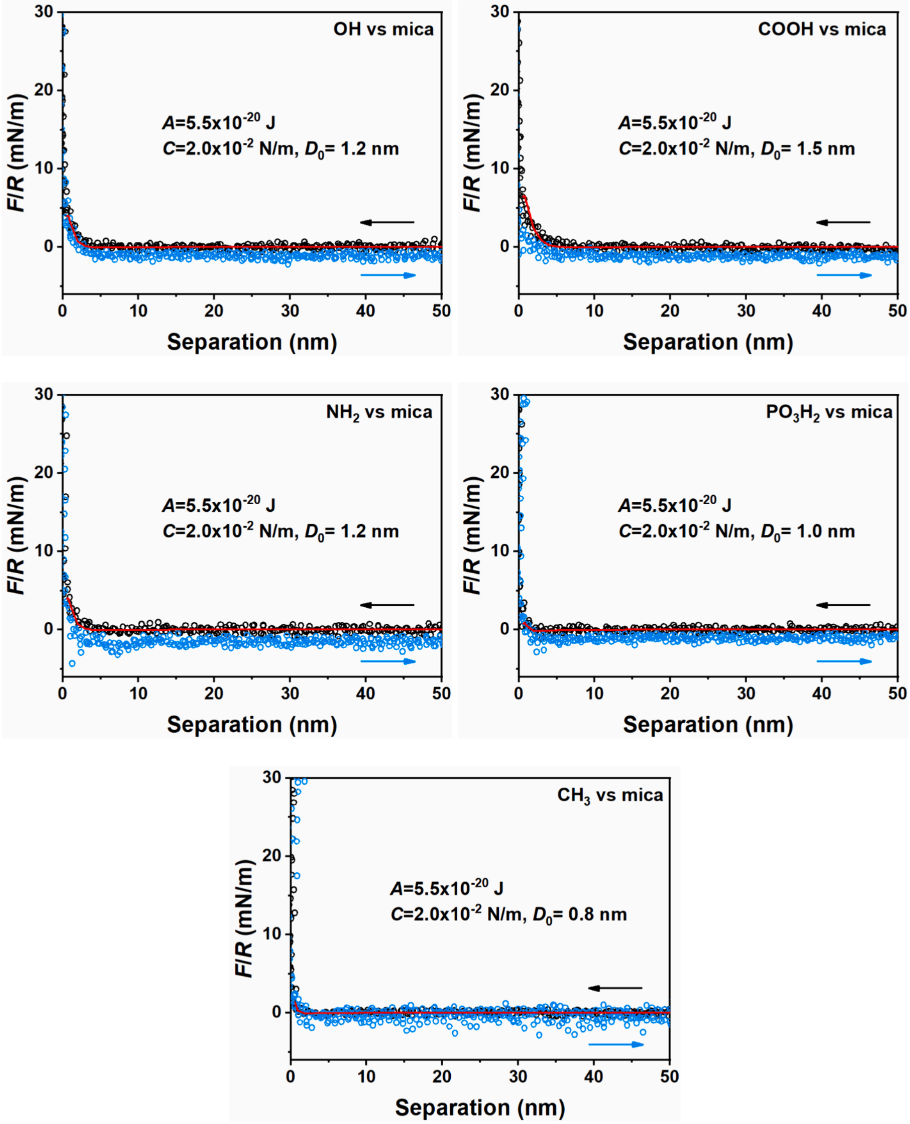

Fig. 7. Typical force-separation curves of interactions between mica surface and functionalized AFM tips in PBS pH 7.4. The circles are the experimental data, and the lines are the theoretical calculation curves. In the theoretical calculation, van der Waals force and hydration force contribute to the total force. The Hamaker constant A=5.5 × 10^{-20} J (Eastman and Zhu, 1996). For the hydration force, the decay length D$_0$ is 1.2 nm for –OH, 1.5 nm for –COOH, 1.2 nm for –NH$_2$, 1.0 nm for –PO$_3$H$_2$, and 0.8 nm for –CH$_3$, and the pre-exponential parameter C is 2.0 × 10^{-2}N/m. Each panel shows five force curves.

-PO$_3$H$_2$ > –CH$_3$. The steric force on mRNA-LNP has a longer range than the hydration force on mica. However, in our work, there is no "breakthrough" force caused by the penetration of the AFM tip into the lipid bilayer, as was observed in the reported works (Szebeni et al., 2023; de Chateauneuf-Randon et al., 2024). This discrepancy could be caused by the larger tip radius of ~30 nm in this study compared to 2–8 nm in the literature. It can be inferred that during the approach of mRNA-LNP to the surface, the steric force impedes the mRNA-LNP attachment, and the strength of this hindrance varies with the functional groups following the trend of –OH<–COOH<–NH$_2$ < -PO$_3$H$_2$ = –CH$_3$. This variation suggests that the intermolecular interactions between the functional groups on the tips and lipid nanoparticle surface play a role in determining the apparent steric force. The overall intermolecular interactions between the functionalized AFM tips and lipid nanoparticles are influenced by various factors, including electrostatic interaction and hydrogen bonding, which affect the conformation of the interacting molecules. The steric force is sensitive to molecular conformations, and thus can be modulated by the functional groups. The role of intermolecular interactions is further elaborated by analyzing adhesion force.

3.4. Adhesion force between mRNA-LNP and functionalized AFM tip

The adhesion force is obtained on the retracting force-separation curve and is useful for the analysis of intermolecular interactions between the mRNA-LNP and functionalized AFM tip. The histograms of normalized adhesion force F_{ad}/R are shown in Fig. 8. Among all the functional groups, –OH has the strongest adhesion with mRNA-LNP ranging from 10 to 45 mN/m having a maximum frequency at ~21.6 mN/m, followed by –COOH having a maximum frequency at ~11.6 mN/m. In the case of the –NH$_2$ functionalized tip, the adhesion is even weaker (maximum frequency at ~5.3 mN/m), while the –PO$_3$H$_2$ and –CH$_3$ have the weakest adhesion with mRNA-LNP. The adhesion sequence is then written as –OH>–COOH>–NH$_2$ > -PO$_3$H$_2$ ≈ –CH$_3$. The variation in adhesion is attributed to the diversity of intermolecular interactions, such as hydrogen bonding and electrostatic interactions, between the functional groups on the AFM tips and mRNA-LNP. The abundant functional groups on the surface of mRNA-LNP, such as the

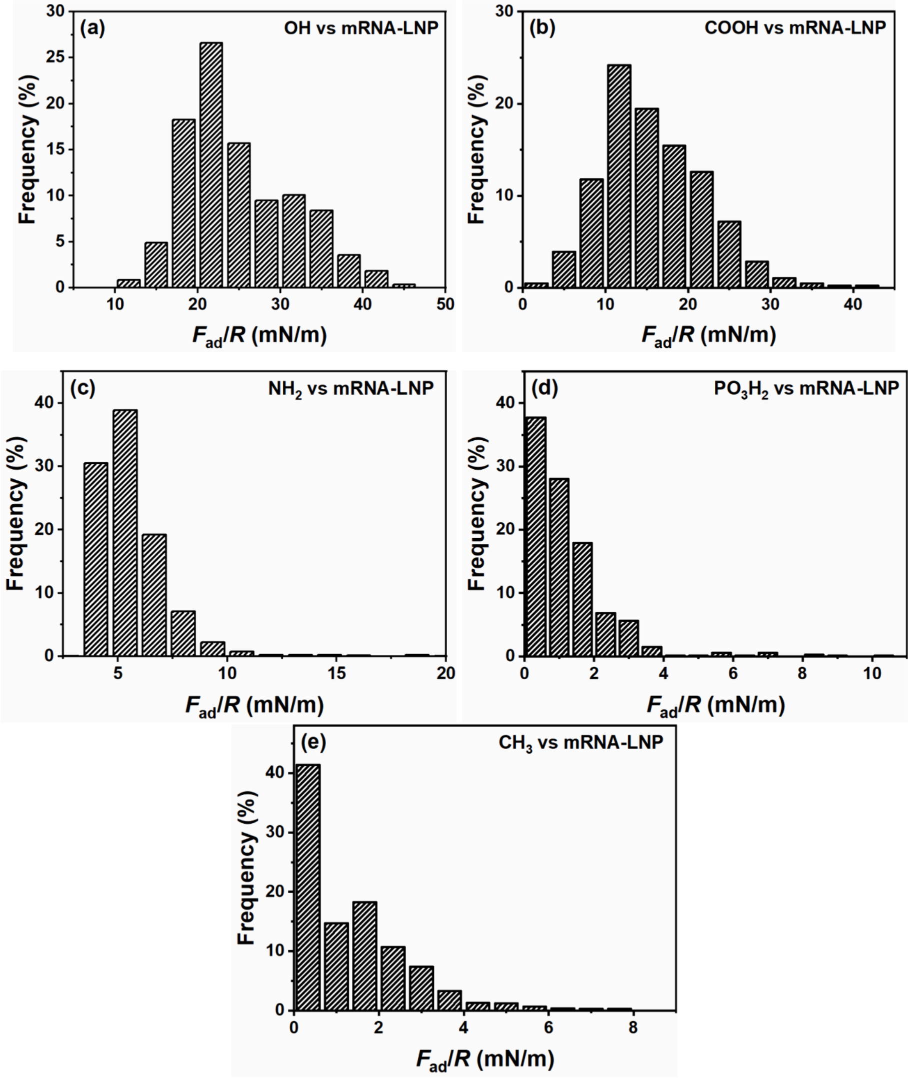

Fig. 8. Adhesion histograms generated from the retracting force-separation curves of the interactions of mRNA-LNP and functionalized AFM tips in PBS pH 7.4 (a) –OH, (b) –COOH, (c) –NH_2, (d) –PO_3H_2 and (e) –CH_3.

quaternary ammonium cation in the distearoylphosphatidylcholine (DSPC) lipid, –OH in the cholesterol, and —O— in the PEG lipid, could form hydrogen bonds with the functionalized AFM tips. The bond strength of O—H⋯O is greater than those of N—H⋯O (David et al., 2017), and therefore the adhesion with the –OH functionalized tip is stronger than that with the –NH_2 functionalized tip. It is noted that, at pH 7.4, the –OH group is negatively charged (Xie et al., 2020; Schollbach et al., 2014), thus the electrostatic repulsion between the –OH functionalized tip and the slightly negatively charged mRNA-LNP (zeta potential ~−8.3 mV in Milli-Q water) could reduce the adhesion. While the –NH_2 group (pKa ~7.3–7.7) (Xie et al., 2020) is nearly neutral or slightly positively charged at pH 7.4, the electrostatic interaction should have negligible influence on the adhesion between the –NH_2 functionalized tip and mRNA-LNP. Although the electrostatic interaction is involved, the adhesion of –OH is still stronger than that of –NH_2, which indicates that the hydrogen bonding dominates the adhesion forces measured by the –OH and –NH_2 functionalized tips. However, this is not the case for the interactions between the functionalized tips and the pure mica surface. As illustrated in Fig. 9, –NH_2 has stronger adhesion with mica (surface potential > -100 mV in water (Pashley and Quirk, 1984) than –OH. Although hydrogen bonding has also been reported to exist on mica surfaces due to the presence of —Si—O— (Urashima et al., 2020; Wu et al., 2017), the results in this work suggest that the electrostatic interaction dominates the adhesion force on the mica surface.

The adhesion force of the –CH_3 functionalized tip with the mRNA-LNP is small, as the hydrogen bond of –CH_3 with the group –NH_2 or –OH in lipid is weak (MacLeod et al., 2011; Brela et al., 2017; Melandri, 2011). While both –COOH and –OH have O—H⋯N and O—H⋯O with mRNA-LNP, the higher negative charge density of –COOH than –OH (Xie et al., 2020) at pH 7.4 induces a larger electrostatic repulsion with mRNA-LNP. Consequently, the adhesion of –COOH is weaker than that of –OH. The −PO_3H_2 has even greater negative charge density as the pKa$_2$ is ~7.7 (Zhang et al., 2000) and each −PO_3H_2 carries 1 to 2 negative charges, so the electrostatic repulsion becomes significant, resulting in an even weaker adhesion than –COOH. By examining the adhesion force on a pure mica surface, –CH_3 has stronger adhesion than –OH, –COOH and −PO_3H_2 as attributed to the weaker electrostatic repulsion between the less negatively charged –CH_3 and mRNA-LNP. The sequence for the adhesion on pure mica surface is then written as –NH_2 > –CH_3 > –OH>–COOH>-PO_3H_2, which follows the negative charge density on those functional groups. Therefore, the electrostatic interaction dominates the adhesion force on mica surface. The adhesion force analysis suggests that hydrogen bonding and electrostatic interaction are in control of the binding of mRNA-LNP on the surfaces, as summarized in Fig. 10. By considering both surface and adhesion forces, the most likely binding site for mRNA-LNP attachment is the –OH group

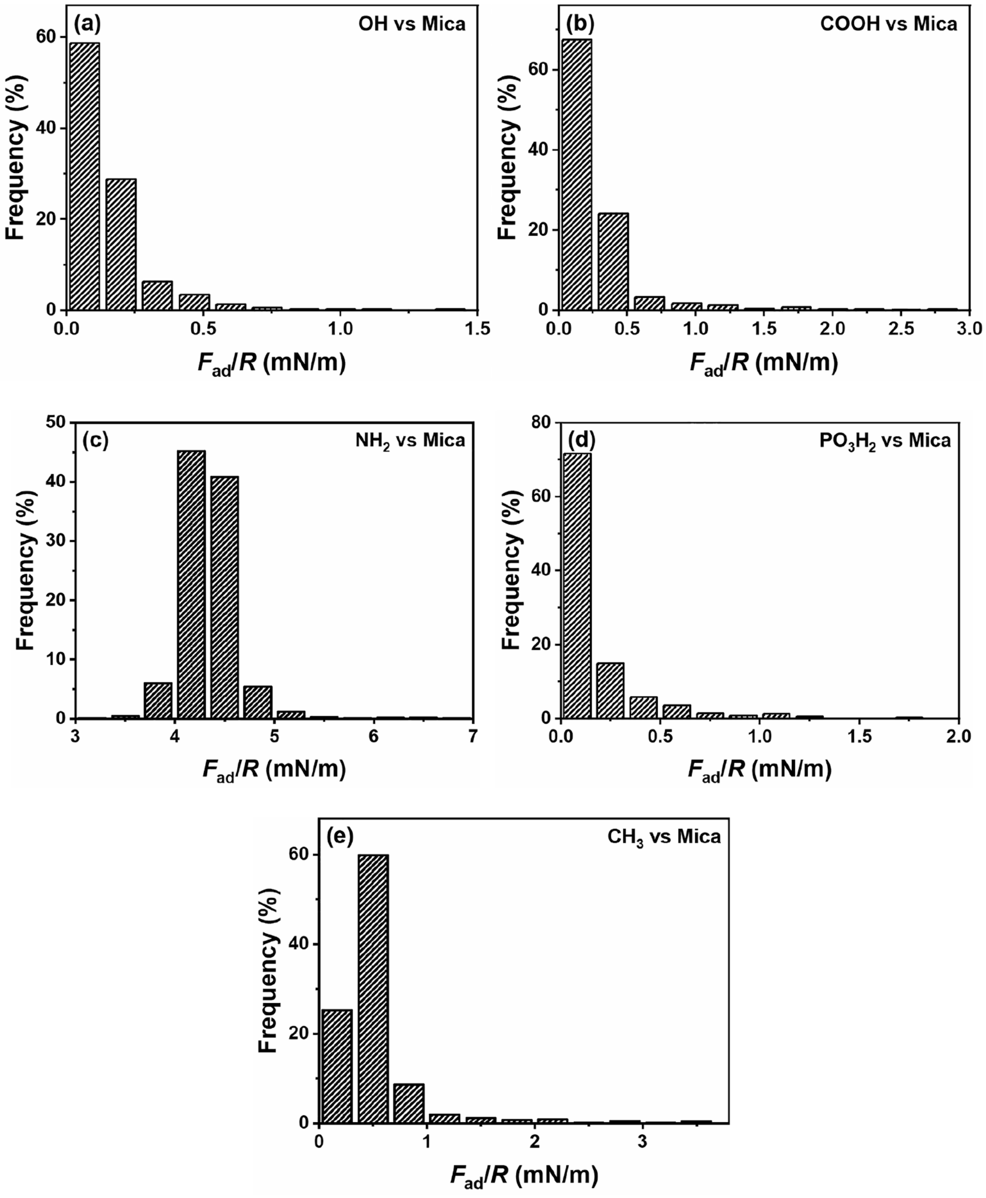

Fig. 9. Adhesion histograms generated from the retracting force-separation curves of the interactions of mica and functionalized AFM tips in PBS pH 7.4 (a) –OH, (b) –COOH, (c) $–NH_2$, (d) $-PO_3H_2$ and (e) $–CH_3$.

in biomolecules such as protein, cholesterol, and carbohydrate, because it exhibits the weakest steric repulsion and the strongest adhesion. The mRNA-LNP could come into contact with other biomolecules and functional surfaces during particle preparation and application, where the interactions between mRNA-LNP and the functional groups would exist. Hence, the proposed mechanism is valid for interactions of mRNA-LNP with a wide range of surfaces possessing the functional groups studied in this work.

4. Conclusions

The morphology and surface structure of mRNA and mRNA-LNP samples have been characterized by cryo-TEM and high-resolution AFM imaging. The mRNA chains are extended with several stacking to form RNA secondary/tertiary structures. After encapsulation in lipid particles, the mRNA molecules adjust their structure to adapt to the spherical/ellipsoidal shape of mRNA-LNP. The surface charge property of mRNA and mRNA-LNP has been determined by the zeta potential measurement, which suggests the screening of negative surface charges of mRNA by, for example, the cationic lipid in LNP. The forces of the interactions between the mRNA-LNP and functional groups in PBS pH 7.4 have been measured using AFM force spectroscopy. The AFM tips were modified with various functional groups, i.e., –COOH, –OH, $–NH_2$, $-PO_3H_2$, and $–CH_3$. The approaching force-separation curves suggest that since the van der Waals force is weak and the electrical double layer force is screened in PBS, the steric repulsive force dominates the surface interaction. The theoretical calculation of the steric force reveals the varied strengths for different functional groups on the AFM tip with the trend of $–OH<–COOH<–NH_2 < -PO_3H_2 = –CH_3$, which implies that the intermolecular forces could play a role in determining the attachment of mRNA-LNP. The subsequent adhesion force mapping and adhesion force distribution analysis show that the adhesion strength follows the trend: $–OH>–COOH>–NH_2 > -PO_3H_2 \approx –CH_3$. The strong hydrogen bonding of –OH and –COOH with mRNA-LNP results in the strongest adhesion. In addition to the hydrogen bonding, the electrostatic interaction, which is repulsive for –OH, –COOH, and $-PO_3H_2$, and attractive for $–NH_2$, also contributes to the measured adhesion with mRNA-LNP. The analysis of both the surface and adhesion forces leads to conclusion that the most

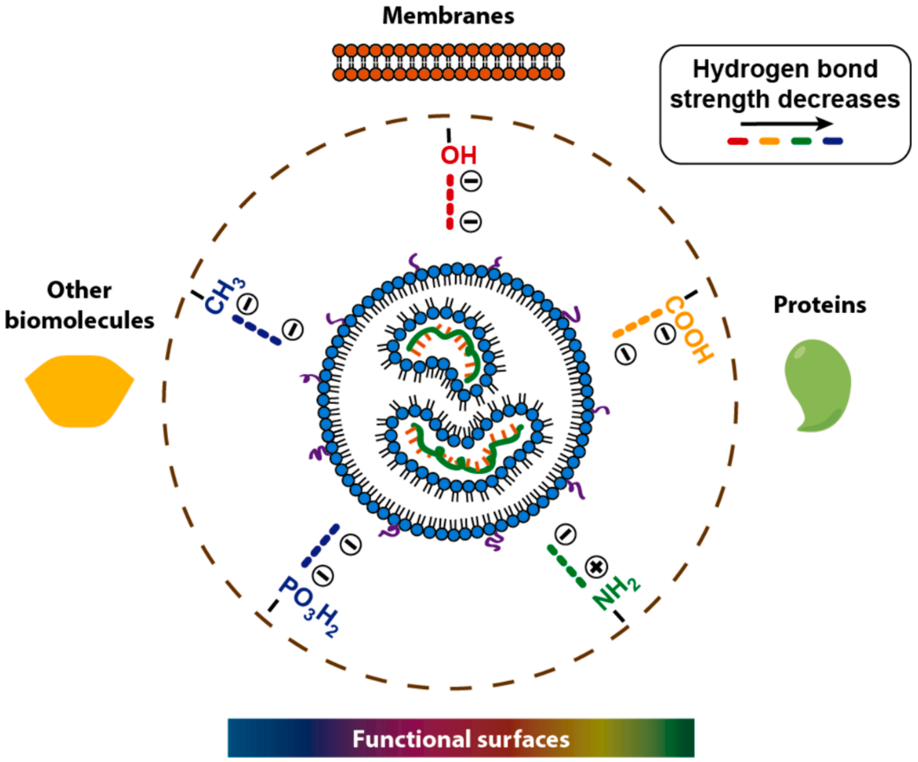

Fig. 10. Schematic of the interaction mechanism of mRNA-LNP with functional groups on biomolecules and functional surfaces. The hydrogen bonding and electrostatic interaction govern the adhesion. The hydrogen bond strength varies and is indicated by different colors.

possible binding site for mRNA-LNP attachment is the –OH group. The adhesion trend of functional groups with mRNA-LNPs help understand the interaction mechanisms of mRNA-LNPs with various surfaces, such as cell membrane, medical device, filtration membrane, etc. It is suggested that the –OH group favors the attachment of mRNA-LNPs, for example, on the carbohydrate at the cell membrane surface. However, the surface of medical device with –OH groups could be fouled by the mRNA-LNPs. The study of interaction mechanisms between mRNA-LNPs and the surfaces with varying functional groups is practical for designing efficient nanocarriers for drug delivery and gene therapy, and has potential applications in the development of functional surfaces to eliminate or enhance the attachment of mRNA-LNPs. The method proposed in this work can be readily extended to investigations of interactions between other biomolecules that occur widely in biological processes.

CRediT authorship contribution statement

Jingyi Wang: Writing – review & editing, Writing – original draft, Methodology, Investigation. **Jiawen Zhang:** Writing – original draft, Validation, Methodology, Investigation. **Sijia Li:** Methodology, Investigation. **Hui Qian:** Resources, Methodology. **Dengfeng Liu:** Resources, Project administration. **Isaias Prado:** Resources, Project administration. **Sharon Wang:** Validation, Project administration. **Akhilesh Bhambhani:** Writing – review & editing, Project administration. **Hongbo Zeng:** Writing – review & editing, Supervision, Conceptualization.

Declaration of competing interest

The authors declare that they have no known competing financial interests or personal relationships that could have appeared to influence the work reported in this paper.

Data availability

Data will be made available on request.

Acknowledgment

This work was supported by the Natural Sciences and Engineering Research Council of Canada (NSERC); the Canada Foundation for Innovation (CFI); and the Canada Research Chairs Program.

Appendix A. Supplementary data

Supplementary data to this article can be found online at https://doi.org/10.1016/j.ces.2024.120693.

References

Apaolaza, P.S., del Pozo-Rodríguez, A., Solinís, M.A., Rodríguez, J.M., Friedrich, U., Torrecilla, J., Weber, B.H.F., Rodríguez-Gascón, A., 2016. Structural recovery of the retina in a retinoschisin-deficient mouse after gene replacement therapy by solid lipid nanoparticles. Biomaterials 90, 40–49.
Brela, M.Z., Boczar, M., Wójcik, M.J., Sato, H., Nakajima, T., Ozaki, Y., 2017. The Born-Oppenheimer molecular simulations of infrared spectra of crystalline poly-(R)-3-hydroxybutyrate with analysis of weak CH···OC hydrogen bonds. Chem. Phys. Lett. 678, 112–118.
Buschmann, M.D., Carrasco, M.J., Alishetty, S., Paige, M., Alameh, M.G., Weissman, D., 2021. Nanomaterial delivery systems for mRNA vaccines. Vaccines 9, 65.
Butt, H.-J., Kappl, M., Mueller, H., Raiteri, R., Meyer, W., Rühe, J., 1999. Steric forces measured with the atomic force microscope at various temperatures. Langmuir 15, 2559–2565.
David, V., Grinberg, N., Moldoveanu, S.C., 2017. Long-Range Molecular Interactions Involved in the Retention Mechanisms of Liquid Chromatography. In: Grushka, E., Grinberg, N. (Eds.), Advances in Chromatography. CRC Press, Boca Raton, p. 82.
de Chateauneuf-Randon, S., Bresson, B., Ripoll, M., Huille, S., Barthel, E., Monteux, C., 2024. The mechanical properties of lipid nanoparticles depend on the type of biomacromolecule they are loaded with. Nanoscale.
del Pozo-Rodríguez, A., Delgado, D., Solinís, M.A., Gascón, A.R., Pedraz, J.L., 2008. Solid lipid nanoparticles for retinal gene therapy: transfection and intracellular trafficking in RPE cells. Int. J. Pharm. 360, 177–183.
Drelich, J., Long, J., Yeung, A., 2007. Determining surface potential of the bitumen-water interface at nanoscale resolution using atomic force microscopy. Can. J. Chem. Eng. 85, 625–634.
Dumitru, A.C., Herruzo, E.T., Rausell, E., Ceña, V., Garcia, R., 2015. Unbinding forces and energies between a siRNA molecule and a dendrimer measured by force spectroscopy. Nanoscale 7, 20267–20276.

Dumitru, A.C., Conrard, L., Lo Giudice, C., Henriet, P., Veiga-da-Cunha, M., Derclaye, S., Tyteca, D., Alsteens, D., 2018. High-resolution mapping and recognition of lipid domains using AFM with toxin-derivatized probes. Chem. Commun. 54, 6903–6906.

Eastman, T., Zhu, D.-M., 1996. Adhesion forces between surface-modified AFM tips and a mica surface. Langmuir 12, 2859–2862.

Frisbie, C.D., Rozsnyai, L.F., Noy, A., Wrighton, M.S., Lieber, C.M., 1994. Functional group imaging by chemical force microscopy. Science 265, 2071–2074.

Gan, L., Wang, J., Zhao, Y., Chen, D., Zhu, C., Liu, J., Gan, Y., 2013. Hyaluronan-modified core–shell liponanoparticles targeting CD44-positive retinal pigment epithelium cells via intravitreal injection. Biomaterials 34, 5978–5987.

Garcia-Manyes, S., Sanz, F., 2010, 1798,. Nanomechanics of lipid bilayers by force spectroscopy with AFM: a perspective, Biochimica et Biophysica Acta (BBA) -. Biomembranes 741–749.

Helm, C.A., Knoll, W., Israelachvili, J.N., 1991. Measurement of ligand-receptor interactions. Proc. Natl. Acad. Sci. 88, 8169–8173.

Hou, X., Zaks, T., Langer, R., Dong, Y., 2021. Lipid nanoparticles for mRNA delivery. Nat. Rev. Mater. 6, 1078–1094.

Hu, W., Xie, L., Zhang, C., Wang, J., Qiao, C., Li, S., Chen, J., Zhao, Z., Zeng, H., 2022. Demystifying constructive strategies on designing functionalized lamellar Nb_2CT_x nanosheet membrane architectures under confined space. J. Mater. Chem. A 10, 4200–4208.

Inkinen, S., Hakkarainen, M., Albertsson, A.-C., Södergård, A., 2011. From Lactic Acid to Poly(lactic acid) (PLA): characterization and Analysis of PLA and Its Precursors. Biomacromolecules 12, 523–532.

Israelachvili, J.N., 1994. Strength of van der Waals Attraction between Lipid Bilayers. Langmuir 10, 3369–3370.

Israelachvili, J.N., 2011. Intermolecular and Surface Forces: Revised, Third Edition. Elsevier Science.

Israelachvili, J.N., Wennerstroem, H., 1992. Entropic forces between amphiphilic surfaces in liquids. J. Phys. Chem. 96, 520–531.

Jeppesen, C., Wong, J.Y., Kuhl, T.L., Israelachvili, J.N., Mullah, N., Zalipsky, S., Marques, C.M., 2001. Impact of polymer tether length on multiple ligand-receptor bond formation. Science 293, 465–468.

Kisby, T., Yilmazer, A., Kostarelos, K., 2021. Reasons for success and lessons learnt from nanoscale vaccines against COVID-19. Nat. Nanotechnol. 16, 843–850.

Kretov, D.A., Curmi, P.A., Hamon, L., Abrakhi, S., Desforges, B., Ovchinnikov, L.P., Pastré, D., 2015. mRNA and DNA selection via protein multimerization: YB-1 as a case study. Nucleic Acids Res. 43, 9457–9473.

Kulkarni, T., Mukhopadhyay, D., Bhattacharya, S., 2022. Influence of surface moieties on nanomechanical properties of gold nanoparticles using atomic force microscopy. Appl. Surf. Sci. 591, 153175.

Kumar, S., Li, M.S., 2010. Biomolecules under mechanical force. Phys. Rep. 486, 1–74.

J. Li, Interactions Between Lipid Membranes and Dendron-Grafted Surfaces, in, Rutgers The State University of New Jersey, School of Graduate Studies, United States – New Jersey, 2017, pp. 39.

MacLeod, J.M., Rosei, F., 2011. 3.02 - Directed Assembly of Nanostructures. In: Andrews, D.L., Scholes, G.D., Wiederrecht, G.P. (Eds.), Comprehensive Nanoscience and Technology. Academic Press, Amsterdam, pp. 13–68.

Mager, M.D., 2009. Interactions between lipid bilayers and inorganic material surfaces, in. Stanford University, United States –, California, p. 112.

Malone, R.W., Felgner, P.L., Verma, I.M., 1989. Cationic liposome-mediated RNA transfection. Proc. Natl. Acad. Sci. 86, 6077–6081.

Melandri, S., 2011. "Union is strength": how weak hydrogen bonds become stronger. Phys. Chem. Chem. Phys. 13, 13901–13911.

Messerian, K.O., Zverev, A., Kramarczyk, J.F., Zydney, A.L., 2023. Characterization and associated pressure-dependent behavior of deposits formed during sterile filtration of mRNA-Lipid nanoparticles. J. Membr. Sci. 684, 121896.

Nakamura, T., Yamada, K., Sato, Y., Harashima, H., 2020. Lipid nanoparticles fuse with cell membranes of immune cells at low temperatures leading to the loss of transfection activity. Int. J. Pharm. 587, 119652.

Neaves, K.J., Huppert, J.L., Henderson, R.M., Edwardson, J.M., 2009. Direct visualization of G-quadruplexes in DNA using atomic force microscopy. Nucleic Acids Res. 37, 6269–6275.

Park, W., Müller, S., Baumann, R.-P., Becker, S., Hwang, B., 2020. Surface energy characterization of nanoscale metal using quantitative nanomechanical characterization of atomic force microscopy. Appl. Surf. Sci. 507, 145041.

Pashley, R.M., Quirk, J.P., 1984. The effect of cation valency on DLVO and hydration forces between macroscopic sheets of muscovite mica in relation to clay swelling. Colloids Surf. 9, 1–17.

Peng, L., Wagner, E., 2019. Polymeric carriers for nucleic acid delivery: current designs and future directions. Biomacromolecules 20, 3613–3626.

Pera, I., Stark, R., Kappl, M., Butt, H.-J., Benfenati, F., 2004. Using the atomic force microscope to study the interaction between two solid supported lipid bilayers and the influence of synapsin I. Biophys. J. 87, 2446–2455.

Qian, H., 2021. Major factors influencing the size distribution analysis of cellulose nanocrystals imaged in transmission electron microscopy. Polymers 13, 3318.

Qian, H., Jia, Y., McCluskie, M.J., 2021. Application of Cryogenic Transmission Electron Microscopy for Evaluation of Vaccine Delivery Carriers. In: Pfeifer, B.A., Hill, A. (Eds.), Vaccine Delivery Technology: Methods and Protocols. Springer, US, New York, NY, pp. 499–511.

Schoenmaker, L., Witzigmann, D., Kulkarni, J.A., Verbeke, R., Kersten, G., Jiskoot, W., Crommelin, D.J.A., 2021. mRNA-lipid nanoparticle COVID-19 vaccines: structure and stability. Int. J. Pharm. 601, 120586.

Schollbach, M., Zhang, F., Roosen-Runge, F., Skoda, M.W.A., Jacobs, R.M.J., Schreiber, F., 2014. Gold nanoparticles decorated with oligo(ethylene glycol) thiols: surface charges and interactions with proteins in solution. J. Colloid Interface Sci. 426, 31–38.

Szebeni, J., Kiss, B., Bozó, T., Turjeman, K., Levi-Kalisman, Y., Barenholz, Y., Kellermayer, M., 2023. Insights into the structure of comirnaty covid-19 Vaccine: a theory on soft, partially bilayer-covered nanoparticles with hydrogen bond-stabilized mRNA–lipid complexes. ACS Nano 17, 13147–13157.

Turasan, H., Kokini, J.L., 2017. Advances in understanding the molecular structures and functionalities of biodegradable Zein-based materials using spectroscopic techniques: a review. Biomacromolecules 18, 331–354.

Urashima, S.-H., Uchida, T., Yui, H., 2020. A hydrogen-bonding structure in self-formed nanodroplets of water adsorbed on amorphous silica revealed via surface-selective vibrational spectroscopy. Phys. Chem. Chem. Phys. 22, 27031–27036.

van Oss, C.J., 2000. Nature of specific ligand-receptor bonds, in particular the antigen-antibody bond. J. Immunoassay 21, 109–142.

Wang, J., Li, J., Xie, L., Shi, C., Liu, Q., Zeng, H., 2016. Interactions between elemental selenium and hydrophilic/hydrophobic surfaces: direct force measurements using AFM. Chem. Eng. J. 303, 646–654.

Wang, J., Xie, L., Zhang, H., Liu, Q., Liu, Q., Zeng, H., 2017. Probing interactions between sphalerite and hydrophobic/hydrophilic surfaces: effect of water chemistry. Powder Technol. 320, 511–518.

Wang, J., Zhang, J., Li, S., Liu, D., Bhambhani, A., Zeng, H., 2023. Characterization of structures and molecular interactions of RNA and lipid carriers using atomic force microscopy. Adv. Colloid Interface Sci. 313, 102855.

Wang, J., Wang, Y., Zhang, K., Liu, X., Zhang, S., Wang, D., Xie, L., 2024. Understanding the role of infusing lubricant composition in the interfacial interactions and properties of slippery surface. J. Colloid Interface Sci. 659, 289–298.

Wong, J.Y., Kuhl, T.L., Israelachvili, J.N., Mullah, N., Zalipsky, S., 1997. Direct measurement of a tethered ligand-receptor interaction potential. Science 275, 820–822.

Wu, J., Liu, F., Yang, H., Xu, S., Xie, Q., Zhang, M., Chen, T., Hu, G., Wang, J., 2017. Effect of specific functional groups on oil adhesion from mica substrate: implications for low salinity effect. J. Ind. Eng. Chem. 56, 342–349.

Xie, L., Wang, J., Shi, C., Cui, X., Huang, J., Zhang, H., Liu, Q., Liu, Q., Zeng, H., 2017. Mapping the nanoscale heterogeneity of surface hydrophobicity on the sphalerite mineral. J. Phys. Chem. C 121, 5620–5628.

Xie, L., Lu, Q., Mao, X., Wang, J., Han, L., Hu, J., Lu, Q., Wang, Y., Zeng, H., 2020. Probing the intermolecular interaction mechanisms between humic acid and different substrates with implications for its adsorption and removal in water treatment. Water Res. 176, 115766.

Yan, Y., Xiong, H., Zhang, X., Cheng, Q., Siegwart, D.J., 2017. Systemic mRNA delivery to the lungs by functional polyester-based carriers. Biomacromolecules 18, 4307–4315.

Yin, H., Kanasty, R.L., Eltoukhy, A.A., Vegas, A.J., Dorkin, J.R., Anderson, D.G., 2014. Non-viral vectors for gene-based therapy. Nat. Rev. Genet. 15, 541–555.

Zhang, R., El-Mayta, R., Murdoch, T.J., Warzecha, C.C., Billingsley, M.M., Shepherd, S.J., Gong, N., Wang, L., Wilson, J.M., Lee, D., Mitchell, M.J., 2021. Helper lipid structure influences protein adsorption and delivery of lipid nanoparticles to spleen and liver. Biomater. Sci. 9, 1449–1463.

L. Zhang, P. Wang, Q. Feng, N. Wang, Z. Chen, Y. Huang, W. Zheng, X. Jiang, Lipid nanoparticle-mediated efficient delivery of CRISPR/Cas9 for tumor therapy, NPG Asia Mater., 9 (2017) e441-e441.

Zhang, Y., Gu, H., Yang, Z., Xu, B., 2003. Supramolecular hydrogels respond to ligand−receptor interaction. J. Am. Chem. Soc. 125, 13680–13681.

Zhang, J., Kirkham, J., Robinson, C., Wallwork, M.L., Smith, D.A., Marsh, A., Wong, M., 2000. Determination of the ionization state of 11-thioundecyl-1-phosphonic acid in self-assembled monolayers by chemical force microscopy. Anal. Chem. 72, 1973–1978.

Zhang, N.-N., Li, X.-F., Deng, Y.-Q., Zhao, H., Huang, Y.-J., Yang, G., Huang, W.-J., Gao, P., Zhou, C., Zhang, R.-R., Guo, Y., Sun, S.-H., Fan, H., Zu, S.-L., Chen, Q., He, Q., Cao, T.-S., Huang, X.-Y., Qiu, H.-Y., Nie, J.-H., Jiang, Y., Yan, H.-Y., Ye, Q., Zhong, X., Xue, X.-L., Zha, Z.-Y., Zhou, D., Yang, X., Wang, Y.-C., Ying, B., Qin, C.-F., 2020. A thermostable mRNA Vaccine against COVID-19. Cell 182, 1271–1283. e1216.